Electrophysiology in small compartments

Madeleine R. Howell[1*], Rosalind J. Xu[1*], Adam, E. Cohen[1,2§]
* Equal contribution

[1] Department of Chemistry and Chemical Biology, Harvard University, Cambridge, Massachusetts, USA
[2] Department of Physics, Harvard University, Cambridge, Massachusetts, USA
[§] cohen@chemistry.harvard.edu

ABSTRACT
Voltage-gated ion channels are found in many membrane-enclosed structures, including synaptic vesicles, endosomes, mitochondria, chloroplasts, viruses and bacteria. In small compartments, assumptions underlying Hodgkin-Huxley-type models must be relaxed: [1] stochastic gating of individual ion channels can substantially change the membrane voltage, even during a single gating event; and [2] ionic currents, even through a single channel, can substantially alter internal ionic concentrations. We adapted conductance-based models to incorporate these effects, and we then simulated voltage dynamics of small vesicles as a function of vesicle radius and channel density. We identified regimes in this parameter space with qualitatively distinct dynamics. We then performed stochastic simulations to explore the role of $Na_V1.5$ in maturation of macrophage endosomes. The stochastic model predicted dramatically different dynamics compared to a classical conductance-based approach. Electrophysiology of small structures can be very different from larger structures, even when ion channel composition and density are preserved.

SIGNIFICANCE
With tools of optical electrophysiology one can measure and perturb membrane voltage in sub-micron structures such as organelles, bacteria, and viruses. These new capabilities motivate a re-examination of the assumptions underlying bioelectrical modeling. This paper provides a framework for predicting and interpreting bioelectrical dynamics in small structures.

KEYWORDS
ion channel stochasticity, Markovian simulations, statistical fluctuations

CLASSIFICATION
Physical and biological sciences (major); Biophysics and computational biology (minor)

INTRODUCTION

Most electrophysiology measurements are performed on large cells such as neurons and cardiomyocytes. Ion channels and pumps are also found in small structures, such as synaptic vesicles (1, 2), endosomes (3), lysosomes (4), mitochondria (5), and chloroplasts (6), as well as in bacteria (7–9), yeast (10), and viruses (10, 11) (**Fig. 1A**). Bioelectrical signals in small compartments are important in driving the ATP synthase in mitochondria (12); driving acidification and cargo uptake in synaptic and endocytic vesicles (2, 13, 14); and acidifying the inside of some virus particles during endocytic uptake (15, 16). Voltage- (17) and mechano-sensitive (8) ion channels play important roles in homeostasis of membrane voltage, pH, and osmotic pressure in bacteria.

Historically, membrane voltage in closed sub-micron compartments has been experimentally inaccessible. Patch pipettes have been used to measure membrane voltage in thin dendritic compartments (18), in axonal boutons (19), and in swollen mitochondria (20) and bacteria (21), but in these experiments the internal ionic contents were typically dialyzed by the pipette filling solution. Many compartments, e.g. intracellular organelles, have remained inaccessible to electrophysiology in their native environments.

Advances in fluorescent voltage indicator proteins (22–27) and dyes (28–31) open the possibility to measure membrane voltage in small compartments (32, 33). Several efforts have targeted voltage indicators to sub-cellular compartments, including mitochondria (34, 35), dendritic spines (36), distal astrocytic processes (37), and lysosomes (14, 38), as well as to individual bacteria (39, 40).

With the ability to measure voltage in small domains comes a need for a corresponding theory. Hodgkin-Huxley and subsequent conductance-based models contain several key assumptions. First, these are mean-field models, i.e. the relevant state-variables describe mean channel conductances; fluctuations about the mean are not considered. Second, for ions other than Ca^{2+}, one typically assumes fixed concentrations on the timescale of individual action potentials (41). Both assumptions break down in small structures.

Many studies have examined the role of channel stochasticity in neural firing, but in this scenario the number of channels is typically large (for reviews see (42–44)), and the channel stochasticity is well described as a perturbation to the Hodgkin-Huxley-like dynamics. In the case of small structures, individual channel gating events can dominate membrane voltage (**Fig. 1B**). Similarly, studies have examined dynamic ion concentration changes in neural (45) and cardiac (46) systems, but usually under the assumption that changes in concentrations are slow compared to individual spikes. This assumption also breaks down in small structures (**Fig. 1C**). Here, we analyze the new effects that emerge in small structures from the interaction of channel stochasticity and dynamic ion concentrations.

RESULTS

Scaling electrophysiology to small systems

Single-channel perturbations to membrane voltage

We begin by examining the relationship between membrane voltage and channel dynamics in small systems. **Fig. 1A** depicts the scale of several electrically excitable biological systems. For simplicity, we consider a spherical membrane-bound compartment (a "vesicle") containing a single ion channel of type *a*, with open-state conductance g_{a}^{0} (pS) and reversal potential E_{a} (mV). Assume the membrane has a specific leak conductance G_0 (pS/μm^2) and a resting potential E_0 (mV). Typically G_0 ~1 pS/μm^2 for neuronal membranes (45). What is the effect of the single channel opening on the membrane potential, V?

If we approximate all the conductances as Ohmic, then a simple circuit analysis shows that the change in steady-state membrane potential upon channel *a* opening is:

$$\Delta V_{\mathrm{ss}} = \frac{g_{\mathrm{a}}^{0}(E_{\mathrm{a}}-E_0)}{g_{\mathrm{a}}^{0}+A\,G_0}, \qquad [1]$$

where A is the surface area of the vesicle (here we assume all ion concentrations are fixed). For example, when $g_{\mathrm{a}}^{0} = A\,G_0$, the voltage swing is half its maximum value: $\Delta V_{\mathrm{ss}} = (E_{\mathrm{a}} - E_0)/2$. Not surprisingly, the single-channel gating has a substantial effect on the steady-state membrane potential when the unit conductance surpasses the resting leak conductance. **Fig. 2A** illustrates this scenario for a canonical Hodgkin-Huxley $\mathrm{Na_V}$ channel.

The leak conductance of a vesicle is proportional to its surface area (assuming a high density of leak channels), while the single-channel conductance is independent of the vesicle surface area. Hence, the crossover between charging regimes (i.e. when $g_{\mathrm{a}}^{0} = A\,G_0$) corresponds to a characteristic vesicle radius, r_{c}. For example, for $G_0 = 1$ pS/μm^2 and a $\mathrm{Na_V}$ channel ($g_{\mathrm{a}}^{0} = 14$ pS) (47), the crossover radius is $r_{\mathrm{c}} = 1.1$ μm. For a BK calcium-activated potassium channel (g_{a}^{0} ~200 pS) (48), $r_{\mathrm{c}} = 4$ μm, while for a homomeric 5-$\mathrm{HT_{3A}}$ receptor ($g_{\mathrm{a}}^{0} = 1$ pS) (49), $r_{\mathrm{c}} = 280$ nm.

Upon opening of a single ion channel (**Fig. 2A**), the RC time constant for the voltage to approach its new steady state is

$$\tau_{\mathrm{V}} = \frac{C_{\mathrm{M}}}{g_{\mathrm{a}}^{0}+A\,G_0}, \qquad [2]$$

where $C_{\mathrm{M}} = A\,c_0$ is the membrane capacitance (specific capacitance c_0 ~10 fF/μm^2), and the denominator is the total membrane conductance. At the crossover radius r_{c} defined above, $\tau_{\mathrm{V}} = \tau_{\mathrm{mem}}/2$, where $\tau_{\mathrm{mem}} = c_0/G_0$ is the intrinsic membrane time constant. For example, for $G_0 =$ 1 pS/μm^2, $\tau_{\mathrm{mem}} = 10$ ms and when $r = r_{\mathrm{c}}$, $\tau_{\mathrm{V}} = 5$ ms. If the single-channel gating events have

duration $\tau_{\text{open}} \gg \tau_{\text{V}}$, then ΔV approaches ΔV_{ss} during a gating event (**Fig. 2A**, blue trace). If $\tau_{\text{open}} \ll \tau_{\text{V}}$, then the amplitude of the voltage fluctuations is suppressed to $\Delta V \approx \Delta V_{\text{ss}} \tau_{\text{open}} / \tau_{\text{V}}$ (**Fig. 2A**, yellow trace).

For big vesicles ($r \gg r_{\text{c}}$), single-channel gating changes steady-state voltage by $\Delta V_{\text{ss}} \approx \frac{g_{\text{a}}^{0}(E_{\text{a}} - E_{0})}{A\, G_{0}}$, with time constant $\tau_{\text{V}} \approx \tau_{\text{mem}}$. Since $g_{\text{a}}^{0} \ll A\, G_{0}$ for big vesicles, ΔV_{ss} is a small perturbation to the resting potential (**Fig. 2A**, orange trace). This corresponds to the situation previously analyzed in models of channel stochasticity in neural firing (42–44, 50–53).

For small vesicles ($r \ll r_{\text{c}}$), single-channel gating brings the voltage close to the reversal potential of channel a, i.e. $\Delta V_{\text{ss}} \approx (E_{\text{a}} - E_{0})$. In this case the time constant is $\tau_{V} \approx \frac{A\, c_{0}}{g_{\text{a}}^{0}} \ll \tau_{\text{mem}}$. For example, upon activation of a single 14 pS channel in a vesicle of $r = 0.1$ μm, the voltage responds with a time constant $\tau_{\text{V}} \approx 10^{-4}$ s (**Fig. 2A**, blue trace). When the channel closes, the voltage relaxes back toward the resting potential with time constant τ_{mem}.

Thus, for sufficiently small structures, the single-channel influence on the membrane voltage can be substantial and the membrane voltage equilibrates faster than the characteristic channel gating times (**Fig. 2B)**. Single ion channels then 'see' their own influence on V_{m} during a stochastic gating event. This self-action changes the statistics of channel fluctuations.

For example, consider a vesicle containing a single Na_{V} channel (Na_{V} model in **Fig. S1**) and a constitutively open 'leak' conductance. Here we assume internal ion concentrations are fixed (an assumption relaxed later). In a large vesicle, spontaneous Na_{V} opening (gating variable m^3: 0 → 1; h: 1) is quickly reversed through deactivation (m^3: 1 → 0, **Fig. 2B**, bottom panel). In a small vesicle, spontaneous Na_{V} opening depolarizes the vesicle to a voltage which favors the open state (**Fig. 2B**, top panel). The channel then remains open until open-state inactivation sets in (h: 1 → 0). **Fig. 2C** shows how voltage self-action prolongs spontaneous Na_{V} open-state fluctuations in small vesicles relative to large vesicles.

In a large vesicle, channel closing after an open-state fluctuation typically resets the gating variables to $m^3 = 0$, $h = 1$. The channel is immediately available to open again. Since single-channel gating has minimal effect on V_{m}, the channel has constant probability of opening per unit time. Thus, the waiting-time distribution is exponentially distributed at short times. Occasionally, open-state fluctuations terminate in an inactivated state ($h = 0$). These rare events lead to a long exponential tail to the waiting time distribution (**Fig. 2D**).

In a small vesicle, an open-state fluctuation induces a large depolarization, which continues to act after the channel has inactivated ($h = 0$). The voltage then relaxes back toward E_{Leak} with time constant τ_{mem} (**Fig. 2B**, top). The time-dependent voltage interacts with the voltage-dependent

gating parameters to produce a complex waiting-time distribution (**Fig. 2D**). As a result of the residual depolarization following an open event, the time-average membrane voltage is more depolarized in small vesicles than in large vesicles (**Fig. 2E**).

If the resting potential, E_{Leak}, is hyperpolarized relative to E_{Window}, the window current regime is wide enough, and the repolarization is slow enough, then the channel may have a high probability to re-open when the voltage nears E_{Window} (**Fig. 2F**). In trajectories simulated with a Na_V model modified to have a large window current, we observed voltage oscillations between E_{Window} and E_{Na}. Occasionally the voltage repolarized below E_{Window} without the channel opening, leading to a quiescent epoch with voltage close to E_{Leak} (**Fig. 2G**). A spontaneous opening event would then re-start the oscillatory dynamics. The membrane voltage thus "chattered" between epochs at E_{Leak} and oscillations between E_{Window} and E_{Na} (**Fig. 2F-G**). Through large V_{m} fluctuations and slow membrane voltage repolarization, small vesicles endow channels with a "memory" of prior gating events, which can lead to a rich repertoire of vesicle size-dependent dynamics.

Single-channel perturbations to concentration

Stochastic channel gating can also affect the ionic contents of the vesicle. To change the membrane voltage by an amount ΔV requires a flux of charge $\Delta Q = C\Delta V$. The ions carrying this charge flow into an internal volume M. Thus, the change in concentration, $\Delta\Gamma = C\Delta V/(z\,F\,M)$, where z is the valence of the charge carrier and F is the Faraday constant. For a spherical vesicle of radius r, we have $C \propto r^2$ while $M \propto r^3$, so $\Delta\Gamma \propto 1/r$, i.e. for a given voltage swing, changes in internal concentration are bigger for smaller vesicles. Numerically, the change in concentration is $\Delta\Gamma = 3.1 \times 10^{-4}\,\Delta V/z\,r$, where V is measured in mV, r in microns, and Γ in mM. For an r = 0.1 μm vesicle with a voltage swing ΔV = 100 mV, the change in concentration due to charging is ~0.3 mM/z, likely important only for Ca^{2+}.

This estimate misses an important factor, however. Simultaneous opening of channels with different reversal potentials leads to steady-state ionic flows. Net current can be approximately zero (so $dV/dt \approx 0$), while distinct ionic species maintain equal and opposite flows, e.g. via balanced Na^+ influx and K^+ efflux. In Appendix 1 we analyze this scenario for a persistent Na^+ current combined with a leak conductance, and we derive the characteristic timescale of changes in $[\text{Na}^+]_{\text{in}}$:

$$\tau_{\text{conc}} = MzF\,\frac{(g_{\text{Na}}+g_{\text{Leak}})}{g_{\text{Na}}g_{\text{Leak}}}\,\frac{[\text{Na}^+]_{\text{in}}(0)}{E_{\text{Na}}-E_{\text{Leak}}}, \qquad [3]$$

where $[\text{Na}^+]_{\text{in}}(0)$ is the initial internal concentration of Na^+ and E_{Na} and E_{Leak} are the initial values of the sodium and leak reversal potentials, respectively. The steady state $[\text{Na}^+]_{\text{in}}$ is reached when the reversal potentials of the Na^+ and leak conductance are the same. The steady-state value of $[\text{Na}^+]_{\text{in}}$ is:

$$[\text{Na}^+]_{\text{in}}(\infty) = [\text{Na}^+]_{\text{in}}(0) + \frac{[\text{Na}^+]_{\text{ext}}[\text{X}]_{\text{in}}(0)-[\text{X}]_{\text{ext}}[\text{Na}^+]_{\text{in}}(0)}{[\text{Na}^+]_{\text{ext}}+[\text{X}]_{\text{ext}}}, \qquad [4]$$

where $[X]_{in}(0)$ is the initial internal concentration of the counterion carried by the leak conductance (e.g. Cl^- or K^+). The external concentrations of ions, $[Na^+]_{ext}$ and $[X]_{ext}$ are assumed to be fixed.

Let us consider the case where a single Na_V channel ($g_{Na_V} = 14\ pS$, E_{Na} = 40 mV) and a single K_V channel (e.g. a delayed rectifier potassium channel, $g_{K_V} = 20$ pS, E_K = -90 mV) are open simultaneously. Then the initial steady-state voltage is -36 mV, the initial steady-state Na^+ current is I_{Na} = -1.1 pA and the initial steady-state K^+ current is I_K = +1.1 pA. In a 1 μm diameter vesicle, these currents correspond to $\frac{d[Na^+]_{in}}{dt} = 21$ mM/s. In a 0.1 μm diameter vesicle, $\frac{d[Na^+]_{in}}{dt}$ is 1000-fold higher, i.e. 21 mM/ms. Thus, a millisecond-duration flicker comprising counter-propagating ionic currents can substantially change the ionic content of a small compartment. **Fig. 3A** shows an example of $[Na^+]_{in}$ dynamics resulting from a charging current $\left(I_{Na} = -C_M \frac{dV}{dt}\right)$ and a persistent current $\left(I_{Na} = -C_M \frac{dV}{dt} - I_K\right)$ during Na_V and K_V gating in a small vesicle**.**

Next, we explore how ion channel stochasticity, self-action on membrane voltage, and ion concentration dynamics influence electrophysiology in small compartments.

Electrophysiology in Hodgkin-Huxley-type model vesicles

We modeled small spherical vesicles with variable densities of Hodgkin-Huxley (HH)-type Na_V and K_V channels (**Fig. 3A**, Methods). For biologically plausible vesicle sizes and channel densities, channel numbers vary by ~7 orders of magnitude (**Fig. 3B**). To restore ionic gradients, we added a Na^+/K^+-ATPase with a biophysically realistic Na^+ and K^+ concentration-dependent pumping rate (54, 55). We added Na^+, K^+, and Cl^- leak conductances to set a resting potential of -68 mV. The Na^+/K^+-ATPase and the leaks were proportional to the membrane area and deterministic. We simulated voltage and concentration dynamics, comparing deterministic and probabilistic Markov models of Na_V and K_V channel gating (Methods). In all simulations we treated internal ion concentrations as dynamic and external ion concentrations as approximately constant.

Spontaneous activity

We simulated trajectories of spontaneous Na_V and K_V channel gating. As expected, the deterministic simulations produced no spontaneous activity, since both Na_V and K_V channels remained closed at the resting membrane potential, -68 mV. In stochastic simulations however, Na_V and K_V channels occasionally fluctuated to the open state. The consequences of these fluctuations depended on vesicle size and channel density.

In small vesicles ($r < 100$ nm), a single Na_V channel opening could depolarize the vesicle enough to activate other Na_V channels, leading to a spike (**Fig. 3C**). The spike waveforms were highly variable, due to the strong contributions of discrete channel gating events. During some spikes the Na_V and K_V currents overlapped, driving rapid ion gradient depletion (**Fig. 3C**, inset, right panel). The amount of ion gradient depletion depended on the overlap of the Na_V and K_V open times.

Smaller vesicles supported longer Na_V channel openings due to voltage self-action (**Fig 2C**) and higher channel densities created more opportunity for Na_V and K_V overlap. This gradient depletion caused a long-lasting decrease in vesicle excitability, restored eventually by the activity of the Na^+/K^+-ATPase (we assume a constant supply of ATP). This depletion-mediated refractory period is distinct from a typical refractory period associated with ion channel recovery kinetics. Gradient depletion diminished spontaneous spike frequency at high channel densities (**Fig 3F-G**, right column)

In larger vesicles ($100\ \text{nm} < r < 1\ \mu\text{m}$), single-channel events typically induced subthreshold depolarization (Na_V) and hyperpolarization (K_V). As channel density increased, these independent single-channel events began to overlap in time, leading to voltage dynamics that resembled an Ornstein-Uhlenbeck process, i.e. diffusion in a parabolic potential. This scenario has previously been studied analytically (42) and numerically (52). When the biased random walk of voltage approached the Na_V activation potential, it triggered spikes which resembled classical action potentials (**Fig 3D-E**). The frequency of these events has been modeled as a Kramers escape process (42).

At constant channel density, the spontaneous firing rate showed a non-monotonic dependence on vesicle size (**Fig 3F**). For small vesicles, an increase in size led to an increase in the number of channels. Since a single stochastic channel gating event was sufficient to trigger a spike, more channels led to a higher spontaneous spike rate. For large vesicles, the influence of single-channel gating events on membrane voltage decreased, so spontaneous spikes became less frequent. This non-monotonic trend is similar to results of numerical simulations by Skaugen and Walløe (52). The largest vesicles ($r > 1\ \mu\text{m}$) were quiescent at all but the highest channel densities.

Evoked activity

We next simulated voltage trajectories in response to constant current injection. To mimic the effect of an electrogenic pump (optogenetic or chemically driven), we made the current proportional to membrane area ($I \approx 2.4 \times 10^3\ \text{fA}/\mu\text{m}^2$). We generated voltage trajectories using both stochastic and deterministic (i.e. HH-like) simulations of channel gating with dynamic internal ion concentrations.

When the number of channels was small, discrete gating events led to substantial deviations between the deterministic and stochastic simulations. Stochastic gating events could lead to spontaneous recovery from depolarization block (**Fig. 4A**), and converted regular spike trains into irregular trains (**Fig. 4B**). As channel number increased, stochastic trajectories came to resemble deterministic trajectories of the same vesicle (**Fig. 4C**). We quantified the similarity between voltage traces for deterministic vs. stochastic simulations via root-mean-square deviation (rmsd) between the autocorrelation functions of the two voltage trajectories (Methods). **Fig. 4D** shows the similarity between deterministic and stochastic simulations as a function of vesicle size and channel density.

We quantified the extent of internal ion concentration changes in the stochastic simulations. The ion gradients were more prone to depletion when the vesicle was smaller and the channel density was higher, as in the simulations in the absence of current injection (**Fig 4E** and **3G**).

Na_v1.5 channels and endosome acidification

Finally, we modeled the effects of nanoscale electrophysiology on macrophage endosome acidification. This acidification is essential for killing of pathogens engulfed by phagocytosis. Macrophage endosomes express Na_V1.5, with C-terminus outside the lumen (inverted relative to Na_V1.5 on the cell membrane). The channel density in endosomes is not known (3), so we simulated vesicles with Na_V1.5 densities (ρ_{Na_V}) between 0 – 6400 μm^{-2}. We assumed radius r = 0.2 μm (56) (**Fig. 5A**), initial membrane potential +19 mV (inside relative to outside), initial pH 6.2, and initial internal Na^+ concentration 100 mM (57, 58). A v-ATPase imports H^+, acidifying the endosome during maturation (59, 60), and ClC-7 contributes a small outward H^+ current (59). The electrophysiological parameters and initial conditions are in **Table S2**. The Na_V1.5 model is described in **Note S2**. It features greater steady-state inactivation at moderate to high voltages compared to the default Na_V model.

In deterministic simulations of endosomes with $\rho_{Na_V} = 6400\ \mu m^{-2}$, the mean number of open Na_V1.5 channels was always much less than 1. We rounded the Na_V conductance to the nearest integer (in units of the open-state conductance), which rounded to zero. Hence, the Na_V channels did not contribute to the deterministic simulations (**Fig. 5B**).

In stochastic simulations at $\rho_{Na_V} = 6400\ \mu m^{-2}$, the Na_V1.5 channels were mostly in the inactive state due to the "felt" voltage of -19 mV (outside relative to inside). Occasionally, a single Na_V1.5 channel fluctuated to the open state. In the $r = 0.2$ μm vesicle, this induced a decrease in membrane voltage (inside relative to outside) of ~21±16 mV (mean ± std amplitude of isolated V_m deflections) since [Na^+] was higher inside the endosome than in the cytoplasm. The voltage dips recovered with time constant ~16±2.4 ms (mean ± std time constant of isolated V_m deflections). The voltage decrease enhanced v-ATPase activity and suppressed the outward H^+ current due to ClC-7 activity, speeding up acidification (**Fig. 5B**). The effect of Na_V1.5 activity on the acidification dynamics became more pronounced as Na_V1.5 channel density increased, since the fraction of time when there was one Na_V1.5 channel open was proportional to the number of Na_V1.5 channels present (**Fig. 5C**).

Fig. 5D shows endosomal pH change as a function of the density of Na_V1.5 channels. In the deterministic simulations, the acidification rate was unaffected by the presence of Na_V1.5, since the average number of open channels was approximately zero. In the stochastic simulations, however, the acidification rate increased as Na_V1.5 channel density increased, due to the Na_V-

induced membrane potential fluctuations. Thus, stochastic channel fluctuations are likely relevant to this important physiological process.

CONCLUSIONS

We demonstrated with simple scaling arguments and stochastic simulations that the kinetics and dynamics of voltage-gated channel behavior can be drastically altered in small compartments. Furthermore, electrolyte gradients in small compartments are prone to depletion when counter-propagating conductances coincide. These effects only become apparent when accounting for fast fluctuations in compartment voltage and electrolyte concentrations.

We then constructed an electrophysiological model that combined stochastic Markovian ion channel dynamics with ion concentration update. At vesicle sizes and ion channel densities corresponding to synaptic vesicles or endosomes, both processes cause deviations from predictions of conductance-based models. We found that small compartments support spontaneous spiking and chattering dynamics at low channel densities. We also observed a novel refractory mechanism whereby coincident Na_V and K_V channel activation were sufficient to deplete electrolyte gradients, leading to epochs of inactivity.

We then investigated the activity and possible role of $Na_V1.5$ in acidification of macrophage late endosomes. In Markov-model-based simulations, stochastic opening of $Na_V1.5$ channels led to fluctuations in the membrane voltage which enhanced the acidification rate. We expect that stochastic ion channel effects may also be important in bacteria, viruses, and other organelles.

Our models are also relevant to partially open small compartments, such as nodes of Ranvier in axons. Simple estimates indicate ~10^4 Na^+ ions imported per Na_V channel per action potential, and ~5,000 Na_V channels per node of Ranvier (61). At an internal volume of ~1 μm^3, the change in internal sodium concentration from a single spike is ~80 mM. This substantially exceeds the initial intracellular concentration of ~10 mM. Thus, the cell must rely on diffusion of Na^+ into the internodal space to restore homeostasis between spikes (the Na^+/K^+-ATPase is too slow to act on the timescale of individual interspike intervals).

While our models only considered changes in internal ion concentration, it would be straightforward to include changes in external concentrations too. Such changes are relevant in tightly packed structures such as the brain, where the extracellular volume is smaller than the intracellular volume. Activity-driven elevations in extracellular K^+ concentration have long been thought to cause spreading depolarization in pathological conditions such as epilepsy and stroke.(62, 63)

Our simple models considered only stochasticity in Na_V and K_V channel gating. However, recent work suggests that stochastic dynamics may be a general feature of membrane pumps and

transporters (64, 65). We expect that the framework presented here will be broadly applicable to predicting and interpreting bioelectrical phenomena in small compartments.

METHODS

All simulations were performed in MATLAB.

Single-channel vesicle model

We examine the interaction between stochastic channel gating and V_m using a single 14 pS conductance Na_V channel in the membrane of a spherical vesicle. The vesicle also contains a non-specific and deterministic leak conductance proportional to vesicle area, with $g_{\text{Leak}} = 1\,\frac{\text{pS}}{\mu\text{m}^2} \times A_{\text{m}}$ and the leak reversal potentials given below. Simulations of vesicle V_m are initialized at E_{Leak}. Because unidirectional single-channel currents do not substantially alter internal electrolyte concentrations, Na^+ and leak reversal potentials are not updated. The Markovian model of stochastic Na_V gating is described below (**Markovian dynamics for voltage-gated ion channels)** and in **Note S1**. To examine the role of window currents on channel behavior, we modify Na_V kinetics to yield a model with substantial window. These modifications are described in **Note S1**.

We simulate [1] V_m in response to a single channel current (**Fig. 2A**); $E_{\text{Leak}} = -93$ mV [2] time-to-close of a channel initialized in the open state (**Fig. 2C**); $E_{\text{Leak}} = -25$ mV, and [3] spontaneous trajectories of channel gating and V_m using either the default Na_V model (**Fig. 2B**), $E_{\text{Leak}} = -25$ mV; or the modified window current model (**Fig. 2G**), $E_{\text{Leak}} = -60$ mV. E_{Leak} of -25 mV in [2] and [3] was chosen such that V_m does not transit the window current regime; to isolate the effect of depolarization on channel kinetics and memory. E_{Leak} of -60 mV in [3] was chosen such that channel activation forced V_m to transit the window regime.

Annotated code for simulating the dynamics in **Fig. 2B, C** and **G** is available at: https://github.com/adamcohenlab/howell2025small-scale-ephys/tree/main/code-single_NaV_vesicles

Hodgkin-Huxley (HH) -type vesicle model

We examine the ensemble effects of stochastic and counter-propagating currents in vesicles with HH-like Na_V, K_V and leak conductances (1). While the original HH model does not explicitly consider intracellular ion concentrations, it can be extended to an ion-specific form (45, 55, 66–71). Following the conventions of Hübel et al., the ion concentrations and reversal potentials are updated at each time step, a Na^+/K^+-ATPase model is added to restore the Na^+/K^+ balance, and the non-specific leak current is rendered ion-specific (45, 55). Na_V and K_V channels are modeled as discrete and stochastic with Markovian dynamics (described in **Markovian dynamics for voltage-gated ion channels**). All other conductances are modeled as continuous and deterministic. A current injection proportional to the extravesicular cation ratio is also added. The formulation is:

$$\frac{dV_m}{dt} = -\frac{1}{C_M}\left(I_{Na^+} + I_{K^+} + I_{Cl^-} \right) \quad [5]$$

$$I_{Na^+} = \left(g_{Na_V} N_{open,Na_V} + g_{Na^+,leak}\right)(V_m - E_{Na^+}) - I_{inj}\frac{[Na^+]_o}{[Na^+]_o + [K^+]_o} + 3I_{pump} \quad [6]$$

$$I_{K^+} = \left(g_{K_V} \cdot N_{open,K_V} + g_{K^+,leak}\right)(V_m - E_{K^+}) - I_{inj}\frac{[K^+]_o}{[Na^+]_o + [K^+]_o} - 2I_{pump} \quad [7]$$

$$I_{Cl^-} = g_{Cl^-,leak}\,(V - E_{Cl^-}) \quad [8]$$

$$I_{pump} = I_{pump,max}\left(1 + e^{\frac{25 - [Na^+]_i}{3}}\right)^{-1}\left(1 + e^{5.5 - [K^+]_o}\right)^{-1} \quad [9]$$

Here V_m is the membrane potential, C_M is the membrane capacitance, E_{ion} is the reversal potential; I_{ion} is the ionic current, I_{inj} is the injection current, I_{pump} is the Na^+/K^+-ATPase current; g_{ion_V} is the conductance of a single voltage-gated channel, N_{open,ion_V} is the number of open channels, $g_{ion,leak}$ is the leakage conductance, $[ion]_i$ is the internal ion concentration, and $[ion]_o$ is the external concentration. All vesicles are modeled as spheres. The electrophysiological parameters and initial conditions of the HH-like vesicle model are in **Table S1** and **Note S1**.

Annotated code to simulate the dynamics in **Fig. 3** and **4** is available at: https://github.com/adamcohenlab/howell2025small-scale-ephys/tree/main/code-HH_neuron_vesicles

To compare dynamics between deterministic and stochastic simulations, we used the autocorrelation of the spike train. We chose this measure because it was not sensitive to the precise spike timing. Our measure of similarity plotted in **Fig. 4D** was: $\left(1 - \frac{rmsd}{rmsd_{max}}\right) \times 100\%$, where rmsd is the root-mean-square deviation between the autocorrelation traces, and $rmsd_{max}$ is the maximum rmsd seen across all vesicle sizes and channel densities.

Endosome model

We study the combined effects of stochastic channel dynamics and ion concentration changes in intracellular endosomes. Carrithers *et al.* reported $Na_V1.5$ channels in macrophage late endosomes, and suggested a role in endosome acidification, a part of endosome maturation (3). The minimal endosome model includes $Na_V1.5$, vacuolar-type H^+ ATPase (v-ATPase), and H^+/Cl^- exchange transporter 7 (ClC-7) (59, 60, 72). The $Na_V1.5$ channels are inserted in an inverted orientation relative to the cell membrane; i.e., the intracellular domain (C-terminus) is facing the outside of the endosome. For ClC-7, a 2:1 Cl^-/H^+ coupling ratio is assumed. The formulation is:

$$\frac{dV_m}{dt} = -\frac{1}{C_m}\left(I_{Na^+} + I_{Cl^-} + I_{H^+} \right) \quad [10]$$

$$I_{Na^+} = g_{Na_V1.5} \cdot N_{open,Na_V1.5} \cdot (V_m - E_{Na^+}) \quad [11]$$

$$I_{Cl^-} = N_{ClC-7} \cdot (2 \cdot I_{ClC-7}) \quad [12]$$

$$I_{H^+} = N_{ClC-7} \cdot I_{ClC-7} - N_{v-ATPase} \cdot I_{v-ATPase} \quad [13]$$

$$I_{ClC-7} = F(V_m, [Cl^-]_i, [Cl^-]_e, [H^+]_i, [H^+]_e) \quad [14]$$

$$I_{v-ATPase} = G(V_m, [H^+]_i, [H^+]_e) \quad [15]$$

In which I_{ClC-7} is the net current through a single ClC-7 channel, $I_{v-ATPase}$ is the single-transporter v-ATPase current; the formulations for F, G (Eq. 14 and 15) come from literature (59, 60); $N_{channel}$ is the number of channels. The electrophysiological parameters and initial conditions of the endosome model are in **Table S2**.

Annotated code to simulate the dynamics in **Fig. 5B** and **C** is available at:
https://github.com/adamcohenlab/howell2025small-scale-ephys/tree/main/code-endosome

Markovian dynamics for voltage-gated ion channels

To facilitate the direct comparison between stochastic and deterministic channel dynamics, Markovian state transition models are used for voltage-gated ion channels in all simulations. The Markovian models for HH neuron Na_V and K_V channels, as well as the $Na_V1.5$ channel, come from literature (42, 52, 72–74). The deterministic channel dynamics formulation is:

$$\frac{dN_k}{dt} = \sum_i \alpha_{i\to k} N_i - \sum_i \alpha_{k\to i} N_k \quad [16]$$

In which N_k is the number of channels in state k and $\alpha_{i\to k}$ is the transition rate from state i to state k ($\alpha_{i\to i} = 0$). Transition rates for all voltage-gated ion channels simulated are provided in **Note S1** and **S2**.

The Gillespie method is used for the stochastic simulations (42, 74). In short, we define the sum of all the transition rates across all channels in a system as λ:

$$\lambda = \sum_k (\sum_i \alpha_{k\to i} N_k) \quad [17]$$

Then the probability that no transition occurs in the system after time *t* follows an exponential distribution:

$$P(t) = \lambda \exp[-\lambda t] \quad [18]$$

A random number is drawn from this distribution to determine the time elapsed before the next transition. Then, a uniform random number is drawn to determine which type of transition in which type of channel occurs, with weight $\alpha_{k\to i} \frac{N_k}{\lambda}$ assigned to each type of transition.

Ion concentration update

The deterministic and stochastic Markovian simulations are performed with intravesicular ion concentrations either fixed or continuously updated. The dynamic ion simulations follow the formalism of Hübel and Dahlem (45, 55). The ionic currents are converted to changes in internal and external concentrations, and the reversal potentials of each ionic species are updated accordingly. For all simulations, the external volume is set to 10^5 μm^3; large enough that extravesicular ion concentrations are approximately constant. The ionic composition of the applied current is set proportional to the extravesicular cation ratio. For endosome simulations, a buffering capacity of 40 $\frac{\mathrm{mM}}{\mathrm{dpH}}$ is assumed in updating the intravesicular H^+ concentration, following literature precedent (75).

Dynamic choice of simulation step size

To accommodate vesicle sizes and ion channel densities that vary across orders of magnitudes, the simulation step size, dt, is chosen dynamically at each step, so that the following criteria are satisfied: 1) $dt < 0.001$ ms 2) $dt < 0.2\ \tau_V$; 3) In a single step, the internal concentration of each ion does not change by more than 2%; 3) In stochastic simulations, if dt chosen from the exponential distribution exceeds the limits set by 1), 2), or 3), then the transition is rejected and the system evolves by the time step dictated by 1), 2), or 3).

In simulations of spontaneous activity in single-channel and HH-type vesicles, constraint 1) was relaxed. This minimized the number of timesteps sampled during quiescent periods in vesicles with few channels.

Vesicle size and channel density scales

For the HH-type vesicle model, a range of physiologically relevant vesicle sizes and ion channel densities are considered (**Fig. 3B**). The vesicle radii were selected to correspond approximately to a synaptic vesicle (r = 0.02 μm) (2, 76); an endosome (r = 0.05 μm) (76); a large endosome or vacuole (r = 0.4 μm) (56); a prokaryotic cell (r = 1 μm); and a eukaryotic cell (r = 10 μm). Ion channel densities were selected as follows: $[Na_V\ K_V] = [80\ 20]$ μm^{-2} is the approximate density on the squid giant axon, (42, 55) and $[Na_V\ K_V] = [800\ 200]$ μm^{-2} is the approximate density on a synaptic vesicle if it contains exactly one copy of the K_V channel. On a synaptic vesicle, the copy numbers of each type of ion channel and transporter are often in the single-digit regime (2, 77–80). The ratio of Na_V to K_V channel was fixed at 4 to 1 across all channel density scales.

For the endosome model, the vesicle radius was 0.2 μm. The density of v-ATPase was estimated to be 700 μm^{-2} and that of ClC-7 was 300 μm^{-2} (59, 75). The density of ClC-7 was adjusted so the initial membrane potential was +19 mV (57). The density of $Na_V1.5$ on macrophage late endosomes is not known. We varied this density across a wide range, from 0 to 6400 μm^{-2}.

Appendix: Effect of single-channel gating on ion concentrations

For concreteness we consider a persistent Na^+ current, though the discussion applies to any persistent current. The rate of change of concentration of Na^+ inside the vesicle is:

$$\frac{d[\mathrm{Na}^+]_{\mathrm{in}}}{dt} = -\frac{i_{\mathrm{Na}}}{M\,z\,F}, \qquad \text{A1}$$

where i_{Na} is the inward Na^+ current, M is the vesicle volume, z is the valence (1 for Na^+) and F is the Faraday constant. The sodium current is:

$$i_{\mathrm{Na}} = g_{\mathrm{Na}}(V - E_{\mathrm{Na}}). \qquad \text{A2}$$

We assume that the voltage reaches steady state fast compared to the concentrations, so $V = V_{\mathrm{ss}}$ and:

$$V_{\mathrm{ss}} = \frac{g_{\mathrm{Na}}E_{\mathrm{Na}} + g_{\mathrm{Leak}}E_{\mathrm{Leak}}}{g_{\mathrm{Na}} + g_{\mathrm{Leak}}}. \qquad \text{A3}$$

Combining Eqs. A1-A3 gives:

$$\frac{d[\mathrm{Na}^+]_{\mathrm{in}}}{dt} = \left(\frac{g_{\mathrm{Na}}g_{\mathrm{Leak}}}{g_{\mathrm{Na}} + g_{\mathrm{Leak}}}\right)\frac{1}{MzF}\,(E_{\mathrm{Na}} - E_{\mathrm{Leak}}). \qquad \text{A4}$$

Finally, the sodium reversal potential changes with time as the internal concentration changes:

$$E_{\mathrm{Na}} = \frac{RT}{zF}\ln\frac{[\mathrm{Na}^+]_{\mathrm{out}}}{[\mathrm{Na}^+]_{\mathrm{in}}}. \qquad \text{A5}$$

Combining A1 – A5 gives an expression for the dynamics of $[\mathrm{Na}^+]_{\mathrm{in}}$:

$$\frac{d[\mathrm{Na}^+]_{\mathrm{in}}}{dt} = \left(\frac{g_{\mathrm{Na}}g_{\mathrm{Leak}}}{g_{\mathrm{Na}} + g_{\mathrm{Leak}}}\right)\frac{1}{MzF}\left(\frac{RT}{zF}\ln\frac{[\mathrm{Na}^+]_{\mathrm{out}}}{[\mathrm{Na}^+]_{\mathrm{in}}} - E_{\mathrm{Leak}}\right). \qquad \text{A6}$$

Equation A6 is nonlinear in $[\mathrm{Na}^+]_{\mathrm{in}}$ and does not have a closed-form analytical solution. Numerical integration yields the time-dependent trajectories of $[\mathrm{Na}^+]_{\mathrm{in}}$ and V. Extrapolating the initial rate of change of $[Na^+]_{in}$ yields Eq. 3 in the main text.

In the case where $g_{\mathrm{Leak}} \propto r^2$ and $M \propto r^3$ (i.e. a constant leak conductance per unit membrane area in a spherical vesicle), then $\frac{d[\mathrm{Na}^+]_{\mathrm{in}}}{dt} \propto -\frac{1}{r}$ for small vesicles ($g^0_{\mathrm{Na}} \gg A\,G_0$) and $\frac{d[\mathrm{Na}^+]_{\mathrm{in}}}{dt} \propto -\frac{1}{r^3}$ for large vesicles ($g^0_{\mathrm{Na}} \ll A\,G_0$).

DATA, MATERIALS, AND SOFTWARE AVAILABILITY

Annotated MATLAB code for stochastic simulations of single-channel vesicles, HH-model vesicles, and macrophage endosomes is provided in a publicly accessible GitHub repository: https://github.com/adamcohenlab/howell2025small-scale-ephys

Simulated data and analysis codes are available upon request.

ACKNOWLEDGEMENTS
We thank Prof. Michael Grabe of UCSF for providing us with the Matlab code for the vesicle-type H^+ ATPase model. This work was supported by a NSF Graduate Research Fellowship (M.R.H.) and NSF Quantum Sensing for Biophysics and Bioengineering (QuBBe) Quantum leap challenge institute (QLCI) grant OMA- 2121044. Components of **Fig 1-3**, **5** and **Note S2** were created in BioRender. Howell, M. (2025) https://BioRender.com/nm7zk94

AUTHOR CONTRIBUTIONS
M.R.H. and R.J.X. performed the simulations. R.J.X, M.R.H., and A.E.C. wrote the manuscript. A.E.C. envisioned and supervised this project.

AUTHOR CONTACT
Madeleine R. Howell: madeleinehowell@fas.harvard.edu
Rosalind J. Xu: j_xu@g.harvard.edu
Adam E. Cohen (corresponding author): cohen@chemistry.harvard.edu

COMPETING INTERESTS
The authors declare no competing interest.

SUPPORTING MATERIAL
Supporting material includes **Note S1-S2**, **Fig. S1**, and **Table S1-S2**.

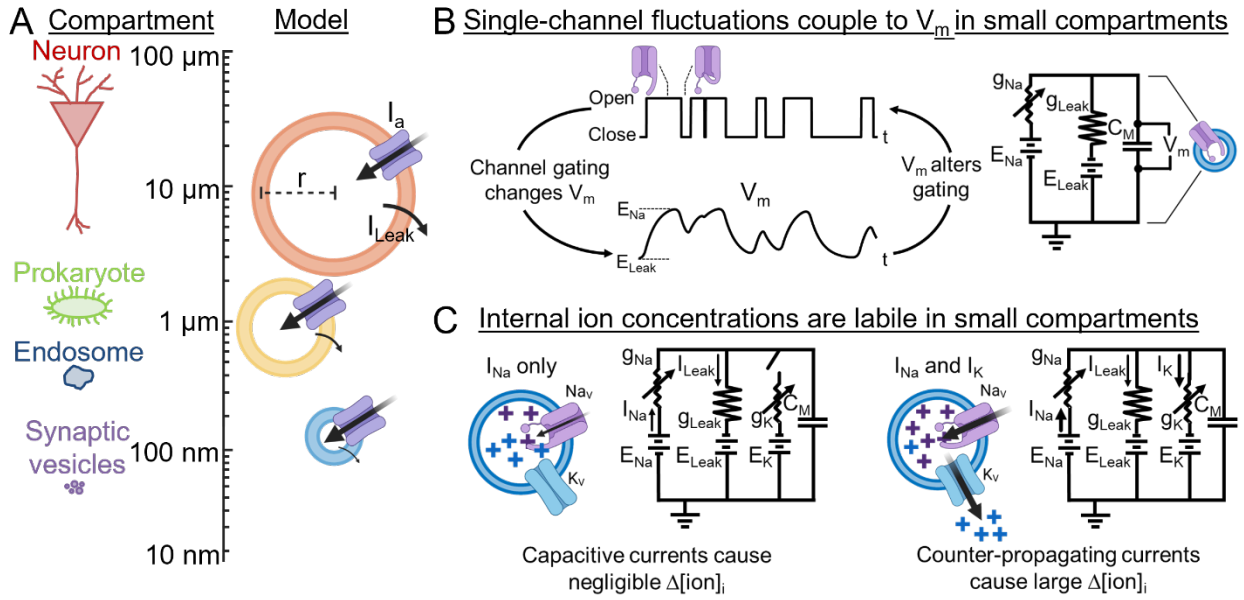

FIGURE 1. Small compartments have distinctive electrophysiology. (**A**) Bioelectrical dynamics occur over a wide range of spatial scales. Excitable compartments (left) and model vesicles with simplified geometry (right). (**B**) Stochastic gating of a single channel changes V_m, which then affects channel gating. Changes in V_m prolong the duration of individual Na_V open events and introduce a coupling between the duration of a gating event and the duration of the subsequent closed epoch. In the circuit diagram the size of the leak resistor indicates $g_{Leak} \ll g_{Na}$. (**C**) Coincident channel activation can drive spontaneous depletion of ionic concentration gradients. Upon Na_V opening, I_{Na} charges the membrane capacitance and then maintains steady-state flow out via I_{Leak} (left panel). For realistic parameters, the capacitive current has negligible effect on internal Na^+ concentration. When Na_V and K_V opening coincide, inward I_{Na} is balanced by outward I_K until E_{Na} and E_K are equal (right panel). This results in large changes to internal electrolyte concentrations. Abbreviations: g_{Na}: Na_V single-channel conductance; g_{Leak}: leak conductance; g_K: K_V single-channel conductance; E_{Na}: Na^+ reversal potential; E_{Leak}: leak reversal potential; E_K: K^+ reversal potential; I_{Na}: Na_V current; I_{Leak}: leak current; I_K: K_V current; C_M: membrane capacitance; V_m: membrane potential.

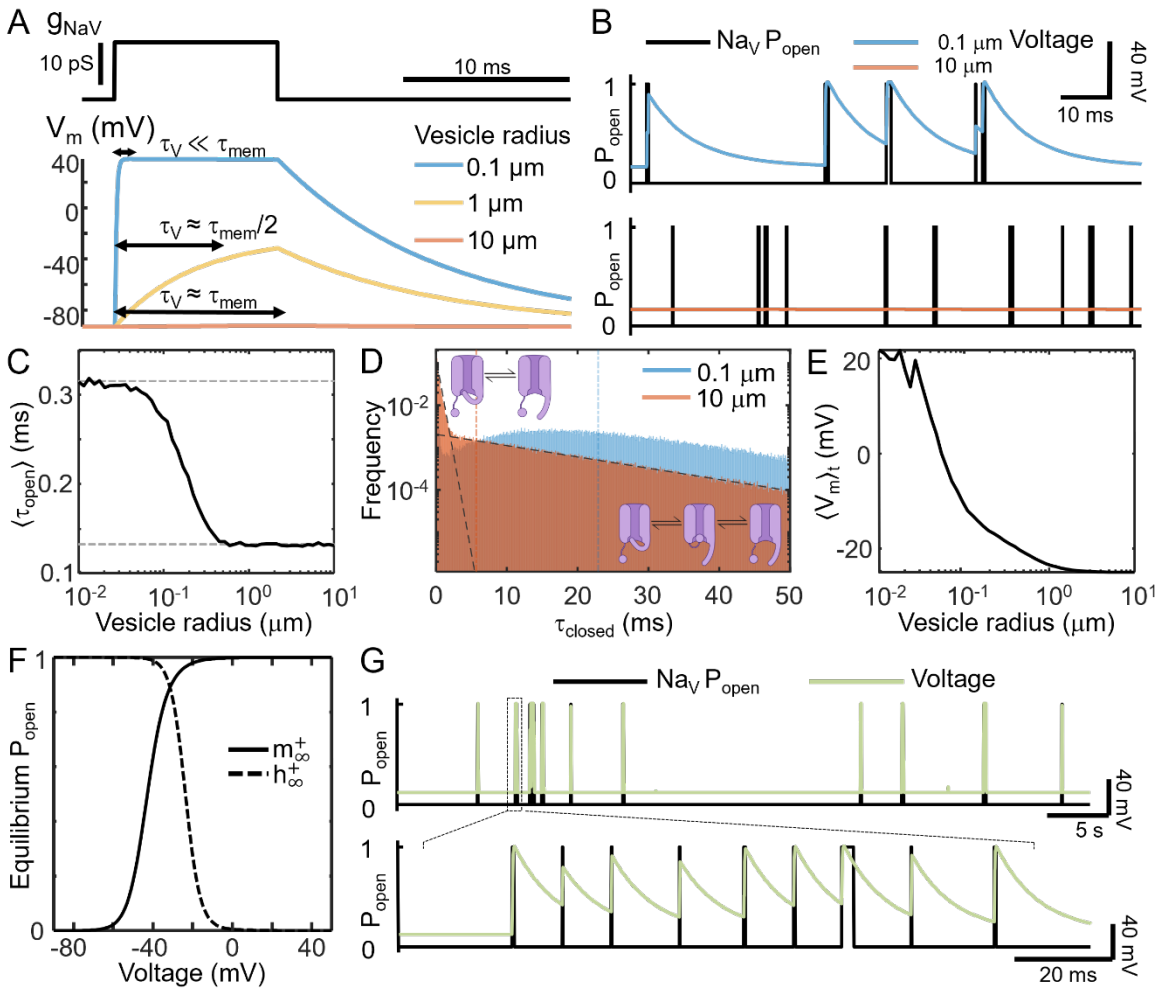

FIGURE 2. Reciprocal interactions between single-channel gating and V_m fluctuations in small compartments. (**A**) Simulated V_m in response to a single Na_V channel opening in vesicles of varying size. τ_V is the time constant of the voltage response when the Na_V channel is open; τ_{mem} is the intrinsic membrane time constant (when the Na_V channel is closed). (**B**) Spontaneous Na_V gating (black) and V_m for $r = 10$ μm (orange) and $r = 0.1$ μm (blue). Leak reversal potential, $E_{Leak} = -25$ mV. (**C**) Mean Na_V open-state dwell time as a function of vesicle radius; average of n = 10^4 simulations of a Na_V channel initialized in the open state at V_m initially at E_{Leak}. Dashed lines show theoretical predictions for the open-state dwell time at $V = E_{Leak}$ (bottom) and $V = E_{Na}$ (top). (**D**) Closed-state dwell time histograms for voltage trajectories in vesicles with $r =$ 10 μm and 0.1 μm, calculated as in **B**; simulations 5,000 s. Gray dashed lines indicate linear fits to the fast $\tau_{closed}^{short} = 1.1 \pm 0.10$ ms (95% confidence) and slow $\tau_{closed}^{long} = 37 \pm 0.20$ ms (95% confidence) closed state dwell times for the $r = 10$ μm vesicle. Orange and blue vertical lines indicate mean τ_{closed} for $r = 10$ μm (5.6 ± 12 ms) and 0.1 μm (23 ± 19 ms) vesicles (mean $\pm$ std). (**E**) Time-average membrane voltage during spontaneous single-channel gating trajectories as in **B**. Each data point is an average of five 50 s-long simulations. (**F**) Steady-state activation (solid trace) and inactivation (dashed) curves for a Na_V model with a large window current. (**G**) Spontaneous Na_V gating (black) and V_m (light green) for the channel model in **F**, for a $r = 0.1$ μm vesicles at $E_{Leak} = -60$ mV. The voltage chatters between epochs of high-frequency oscillation and quiescent epochs.

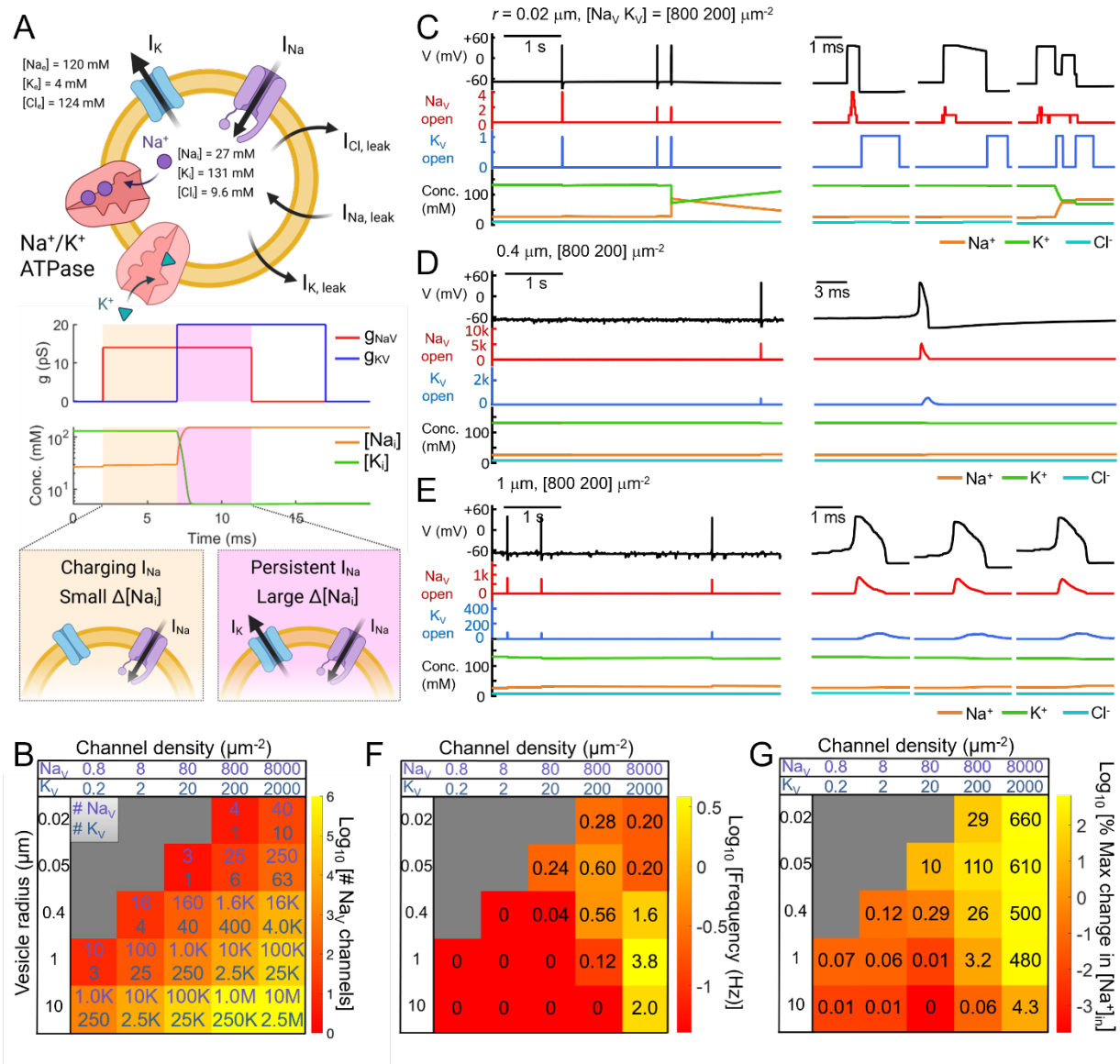

FIGURE 3. Spontaneous voltage dynamics in small compartments. Voltage and ion concentration dynamics were simulated in vesicles with different sizes and channel densities. (**A**) Model vesicle with HH-type conductances and Na^+/K^+-ATPase (top). Activation of an individual Na_V channel does not appreciably change internal [Na^+] (beige panels). Concurrent Na_V and K_V activation depletes [Na^+] and [K^+] concentration gradients until the Na^+ and K^+ reversal potentials become equal (pink panels). Plots are for an $r = 0.02$ μm vesicle. (**B**) Range of vesicle sizes and channel densities investigated. Gray regions correspond to size and density combinations with less than one K_V channel per vesicle. (**C**) Left: 5 s simulation of a vesicle with $r = 0.02$ μm and [Na_V, K_V] = [800, 200] μm^2, corresponding to 4 Na_V channels and 1 K_V channel. Right: close-up of the three spontaneous events. In the third event, Na_V and K_V channel activation overlapped in time, leading to partial dissipation of the ionic gradients. (**D**) Left: 5 s simulation of a vesicle with r = 0.4 μm and [Na_V, K_V] = [800 200] μm^2, corresponding to 1,600 Na_V channels and 400 K_V channels. Overlapping spontaneous Na_V activations were sufficient to trigger well-defined spikes. Changes

in internal ionic composition were small, on account of the larger vesicle size compared to **C**. (**E**) 5 s simulation of a vesicle with r = 1 μm and [Na_V, K_V] = [800 200] μm^2, corresponding to 10,000 Na_V and 2,500 K_V channels. Due to the larger vesicle size, the influence of each gating event diminished compared to the vesicle in **D**. Channel noise led to small fluctuations in baseline voltage, which occasionally triggered spontaneous spikes. (**F**) Color map of average spontaneous spiking frequency as a function of vesicle radius and channel density. (**G**) Color map of the average percent amplitude of internal [Na^+] concentration changes as a function of vesicle radius and channel density. These fluctuations were driven by overlapping Na_V and K_V currents. Data in **F** and **G** are the mean of five, 5 s simulations, excluding the r = 10 μm and [Na_V, K_V] = [8000 2000] μm^2 vesicle, which was simulated for 500 ms due to computational constraints.

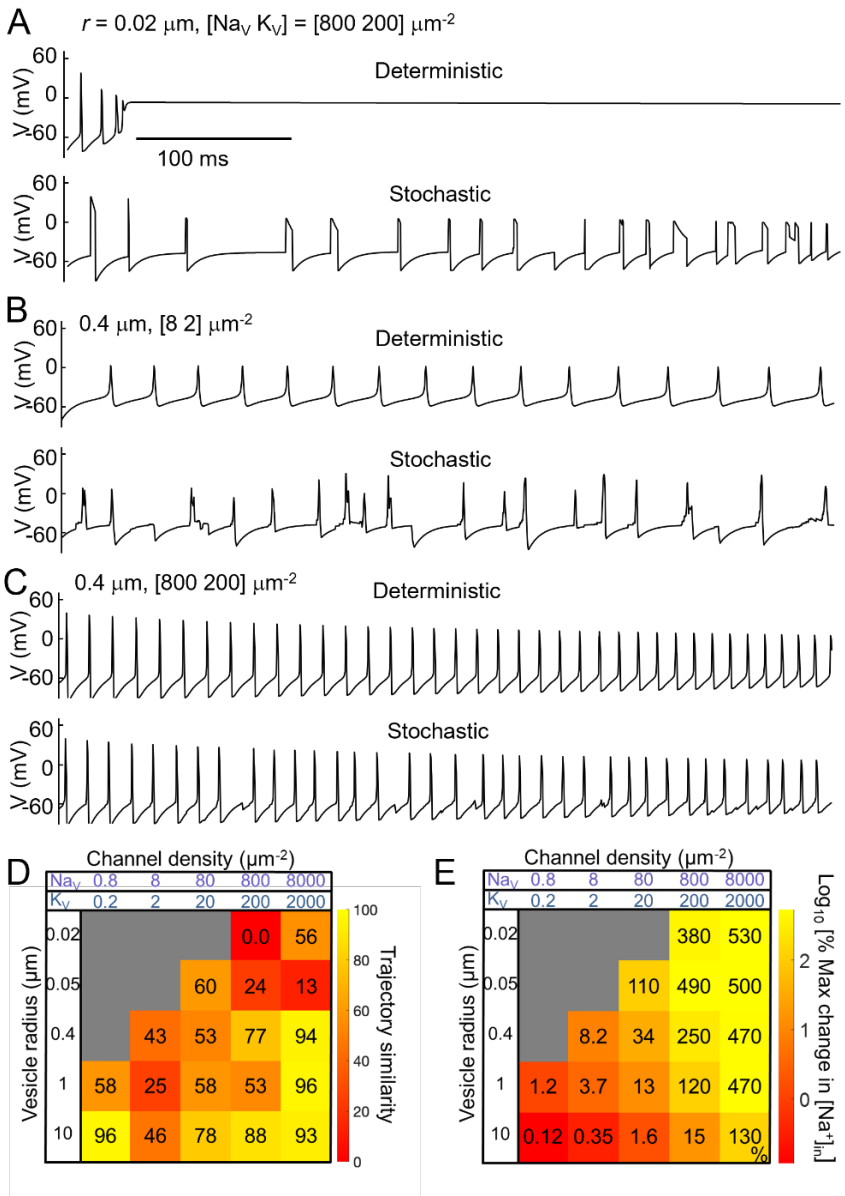

FIGURE 4. Driven voltage dynamics in small compartments. Simulations were performed as in **Fig. 3**, with the addition of a constant inward current density (Methods). (**A**) At the smallest vesicle size, the deterministic simulation quickly entered depolarization block. In the stochastic simulations, fluctuations in channel gating restored the voltage from depolarization block, leading to sustained, but erratic, spiking. (**B**) In an $r = 0.4$ μm vesicle with low channel density, the evoked spikes were variable in waveform due to stochastic variations in the number and timing of channel opening. (**C**) In an $r = 0.4$ μm vesicle with higher channel density, stochastic channel fluctuations caused spike timing to be more variable than in deterministic simulations. (**D**) Color map of the similarity between stochastic and deterministic responses to current injection, as measured by cross-correlation (Methods). In the gray region, there is less than one K_V channel. (**E**) Color map of the percent amplitude of internal $[Na^+]$ concentration changes as a function of vesicle radius

and channel density. Data in **D** and **E** are from one, 5 s simulation, excluding the r = 10 μm and [Na_V, K_V] = [8000 2000] μm^2 vesicle, which was simulated for 500 ms.

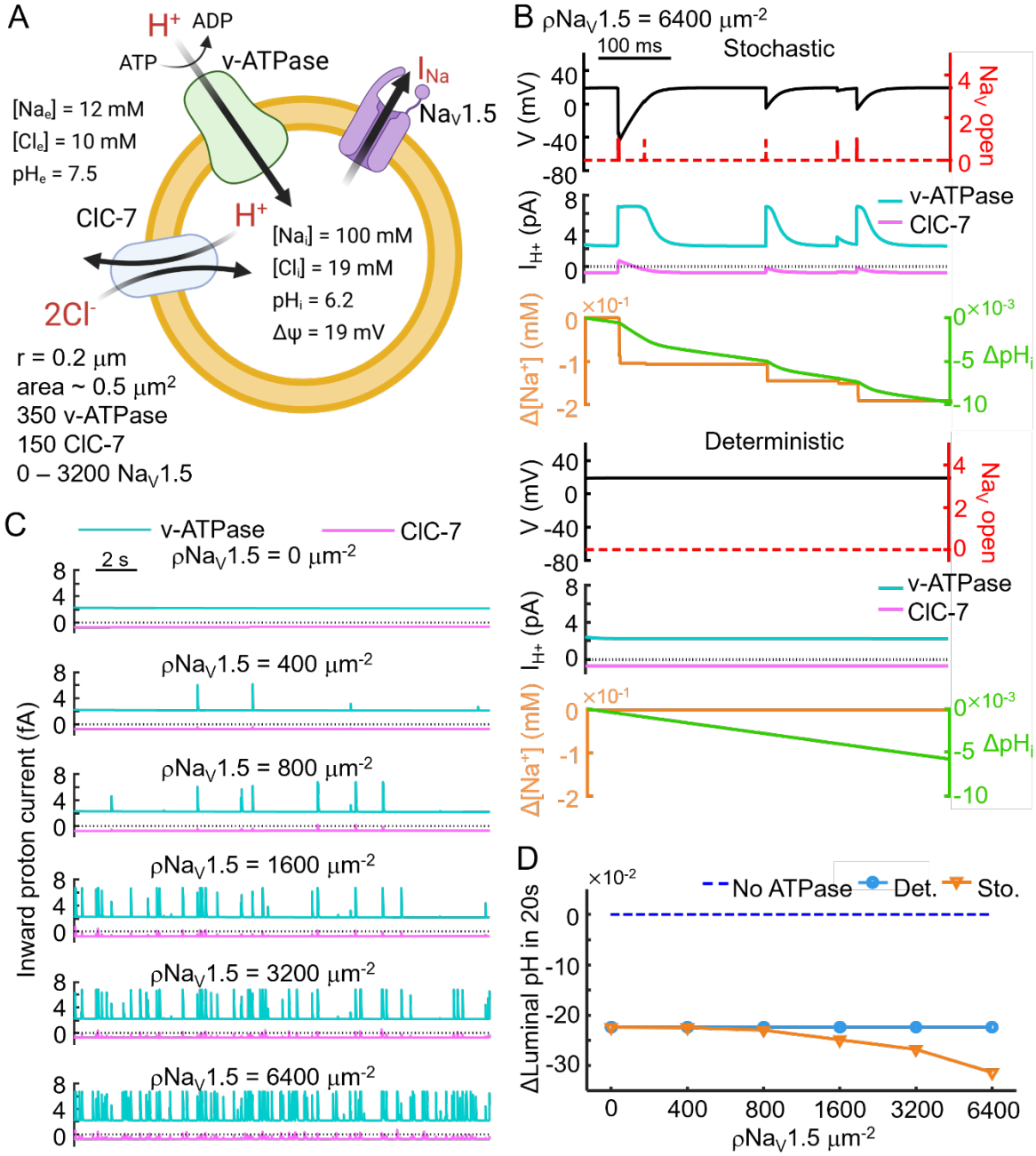

FIGURE 5. Stochastic simulations of endosome acidification dynamics. (**A**) Model endosome. (**B**) Comparison between the stochastic (top) and deterministic (bottom) dynamics. In the stochastic simulation, spontaneous $Na_V1.5$ fluctuations transiently decreased the membrane voltage and increased the acidification rate. (**C**) The effect of $Na_V1.5$ activity on endosome acidification increased at higher $Na_V1.5$ density. (**D**) Luminal pH in stochastic or deterministic simulations after 20 s, across a range of $Na_V1.5$ channel densities. The initial pH is shown as a dashed line.

REFERENCES

1. Rahamimoff, R., S.A. DeRiemer, B. Sakmann, H. Stadler, and N. Yakir. 1988. Ion channels in synaptic vesicles from Torpedo electric organ. *Proceedings of the National Academy of Sciences*. 85:5310–5314.

2. Takamori, S., M. Holt, K. Stenius, E.A. Lemke, M. Grønborg, D. Riedel, H. Urlaub, S. Schenck, B. Brügger, P. Ringler, S.A. Müller, B. Rammner, F. Gräter, J.S. Hub, B.L.D. Groot, G. Mieskes, Y. Moriyama, J. Klingauf, H. Grubmüller, J. Heuser, F. Wieland, and R. Jahn. 2006. Molecular Anatomy of a Trafficking Organelle. *Cell*. 127:831–846.

3. Carrithers, M.D., S. Dib-Hajj, L.M. Carrithers, G. Tokmoulina, M. Pypaert, E.A. Jonas, and S.G. Waxman. 2007. Expression of the Voltage-Gated Sodium Channel NaV1.5 in the Macrophage Late Endosome Regulates Endosomal Acidification1. *The Journal of Immunology*. 178:7822–7832.

4. Wang, W., X. Zhang, Q. Gao, M. Lawas, L. Yu, X. Cheng, M. Gu, N. Sahoo, X. Li, P. Li, S. Ireland, A. Meredith, and H. Xu. 2017. A voltage-dependent K+ channel in the lysosome is required for refilling lysosomal Ca2+ stores. *Journal of Cell Biology*. 216:1715–1730.

5. Ichas, F., L.S. Jouaville, and J.-P. Mazat. 1997. Mitochondria Are Excitable Organelles Capable of Generating and Conveying Electrical and Calcium Signals. *Cell*. 89:1145–1153.

6. Finazzi, G., D. Petroutsos, M. Tomizioli, S. Flori, E. Sautron, V. Villanova, N. Rolland, and D. Seigneurin-Berny. 2015. Ions channels/transporters and chloroplast regulation. *Cell Calcium*. 58:86–97.

7. Martinac, B., M. Buechner, A.H. Delcour, J. Adler, and C. Kung. 1987. Pressure-sensitive ion channel in Escherichia coli. *Proc Natl Acad Sci U S A*. 84:2297–2301.

8. Berrier, C., M. Besnard, B. Ajouz, A. Coulombe, and A. Ghazi. 1996. Multiple Mechanosensitive Ion Channels from Escherichia coli, Activated at Different Thresholds of Applied Pressure. *J. Membrane Biol.* 151:175–187.

9. Radchenko, M.V., K. Tanaka, R. Waditee, S. Oshimi, Y. Matsuzaki, M. Fukuhara, H. Kobayashi, T. Takabe, and T. Nakamura. 2006. Potassium/Proton Antiport System of *Escherichia coli**. *Journal of Biological Chemistry*. 281:19822–19829.

10. Martinac, B., Y. Saimi, and C. Kung. 2008. Ion channels in microbes. *Physiol.Rev.* 88:1449.

11. Sze, C., and Y.-J. Tan. 2015. Viral Membrane Channels: Role and Function in the Virus Life Cycle. *Viruses*. 7:3261–3284.

12. Sorgato, M.C., B.U. Keller, and W. Stühmer. 1987. Patch-clamping of the inner mitochondrial membrane reveals a voltage-dependent ion channel. *Nature*. 330:498–500.

13. Scott, C.C., and J. Gruenberg. 2011. Ion flux and the function of endosomes and lysosomes: pH is just the start. *BioEssays*. 33:103–110.

14. Modi, S., S. M. G., D. Goswami, G.D. Gupta, S. Mayor, and Y. Krishnan. 2009. A DNA nanomachine that maps spatial and temporal pH changes inside living cells. *Nature Nanotech*. 4:325–330.

15. Pinto, L.H., L.J. Holsinger, and R.A. Lamb. 1992. Influenza virus M2 protein has ion channel activity. *Cell*. 69:517–528.

16. Akole, A., and J.M. Warner. 2019. Model of influenza virus acidification. *PLOS ONE*. 14:e0214448.

17. Payandeh, J., and D.L. Minor. 2015. Bacterial Voltage-Gated Sodium Channels (BacNaVs) from the Soil, Sea, and Salt Lakes Enlighten Molecular Mechanisms of Electrical Signaling and Pharmacology in the Brain and Heart. *Journal of Molecular Biology*. 427:3–30.

18. Davie, J.T., M.H.P. Kole, J.J. Letzkus, E.A. Rancz, N. Spruston, G.J. Stuart, and M. Häusser. 2006. Dendritic patch-clamp recording. *Nat Protoc*. 1:1235–1247.

19. Novak, P., J. Gorelik, U. Vivekananda, A.I. Shevchuk, Y.S. Ermolyuk, R.J. Bailey, A.J. Bushby, G.W.J. Moss, D.A. Rusakov, D. Klenerman, D.M. Kullmann, K.E. Volynski, and Y.E. Korchev. 2013. Nanoscale-Targeted Patch-Clamp Recordings of Functional Presynaptic Ion Channels. *Neuron*. 79:1067–1077.

20. Kumari, A., D.M. Nguyen, and V. Garg. 2023. Patch-clamp technique to study mitochondrial membrane biophysics. *Journal of General Physiology*. 155:e202313347.

21. Martinac, B., P.R. Rohde, C.G. Cranfield, and T. Nomura. 2013. Patch Clamp Electrophysiology for the Study of Bacterial Ion Channels in Giant Spheroplasts of E. coli. In: Delcour AH, editor. Bacterial Cell Surfaces: Methods and Protocols. Totowa, NJ: Humana Press. pp. 367–380.

22. Adam, Y., J.J. Kim, S. Lou, Y. Zhao, M.E. Xie, D. Brinks, H. Wu, M.A. Mostajo-Radji, S. Kheifets, V. Parot, S. Chettih, K.J. Williams, B. Gmeiner, S.L. Farhi, L. Madisen, E.K. Buchanan, I. Kinsella, D. Zhou, L. Paninski, C.D. Harvey, H. Zeng, P. Arlotta, R.E. Campbell, and A.E. Cohen. 2019. Voltage imaging and optogenetics reveal behaviour-dependent changes in hippocampal dynamics. *Nature*. 569:413–417.

23. Tian, H., H.C. Davis, J.D. Wong-Campos, P. Park, L.Z. Fan, B. Gmeiner, S. Begum, C.A. Werley, G.B. Borja, H. Upadhyay, H. Shah, J. Jacques, Y. Qi, V. Parot, K. Deisseroth, and A.E. Cohen. 2023. Video-based pooled screening yields improved far-red genetically encoded voltage indicators. *Nat Methods*. 20:1082–1094.

24. Abdelfattah, A.S., J. Zheng, A. Singh, Y.-C. Huang, D. Reep, G. Tsegaye, A. Tsang, B.J. Arthur, M. Rehorova, C.V.L. Olson, Y. Shuai, L. Zhang, T.-M. Fu, D.E. Milkie, M.V. Moya, T.D. Weber, A.L. Lemire, C.A. Baker, N. Falco, Q. Zheng, J.B. Grimm, M.C. Yip, D. Walpita, M. Chase, L. Campagnola, G.J. Murphy, A.M. Wong, C.R. Forest, J. Mertz, M.N. Economo, G.C. Turner, M. Koyama, B.-J. Lin, E. Betzig, O. Novak, L.D. Lavis, K. Svoboda, W. Korff, T.-W. Chen, E.R. Schreiter, J.P. Hasseman, and I. Kolb. 2023. Sensitivity optimization of a rhodopsin-based fluorescent voltage indicator. *Neuron*.

25. Lu, X., Y. Wang, Z. Liu, Y. Gou, D. Jaeger, and F. St-Pierre. 2023. Widefield imaging of rapid pan-cortical voltage dynamics with an indicator evolved for one-photon microscopy. *Nat Commun*. 14:6423.

26. Hao, Y.A., S. Lee, R.H. Roth, S. Natale, L. Gomez, J. Taxidis, P.S. O'Neill, V. Villette, J. Bradley, Z. Wang, D. Jiang, G. Zhang, M. Sheng, D. Lu, E. Boyden, I. Delvendahl, P. Golshani, M. Wernig, D.E. Feldman, N. Ji, J. Ding, T.C. Südhof, T.R. Clandinin, and M.Z. Lin. 2024. A fast and responsive voltage indicator with enhanced sensitivity for unitary synaptic events. *Neuron*. 112:3680-3696.e8.

27. Kannan, M., G. Vasan, S. Haziza, C. Huang, R. Chrapkiewicz, J. Luo, J.A. Cardin, M.J. Schnitzer, and V.A. Pieribone. 2022. Dual-polarity voltage imaging of the concurrent dynamics of multiple neuron types. *Science*. 378:eabm8797.

28. Miller, E.W., J.Y. Lin, E.P. Frady, P.A. Steinbach, W.B. Kristan, and R.Y. Tsien. 2012. Optically monitoring voltage in neurons by photo-induced electron transfer through molecular wires. *Proc.Natl.Acad.Sci.U.S.A.* 109:2114–2119.

29. Navarro, M.X., N.C. Gerstner, S.M. Lipman, G.E. Dolgonos, and E.W. Miller. 2024. Improved Sensitivity in a Modified Berkeley Red Sensor of Transmembrane Potential. *ACS Chem. Biol.* 19:2214–2219.

30. Antic, S.D., P. Yan, C.D. Acker, O.T. Spagnola, Z.Y. Erol, O. Baser, and L.M. Loew. ElectroFluor Voltage-Sensitive Dyes: Comprehensive Analysis of Wavelength-Dependent Sensitivity and Cross-Channel Bleed-Through. *Journal of Biophotonics*. n/a:e70008.

31. Yan, P., C.D. Acker, V. Biasci, G. Judge, A. Monroe, L. Sacconi, and L.M. Loew. 2023. Near-infrared voltage-sensitive dyes based on chromene donor. *Proceedings of the National Academy of Sciences*. 120:e2305093120.

32. Cohen, A.E., and V. Venkatachalam. 2014. Bringing bioelectricity to light. *Annu. Rev. Biophys.* 43:11.1-11.22.

33. Sepehri Rad, M., L.B. Cohen, O. Braubach, and B.J. Baker. 2018. Monitoring voltage fluctuations of intracellular membranes. *Sci Rep*. 8:6911.

34. Crowley, L.C., M.E. Christensen, and N.J. Waterhouse. 2016. Measuring Mitochondrial Transmembrane Potential by TMRE Staining. *Cold Spring Harb Protoc*. 2016.

35. Kowaltowski, A.J., and F. Abdulkader. 2024. How and when to measure mitochondrial inner membrane potentials. *Biophysical Journal*. 123:4150–4157.

36. Cornejo, V.H., N. Ofer, and R. Yuste. 2021. Voltage compartmentalization in dendritic spines in vivo. *Science*. 375:eabg0501.

37. Armbruster, M., S. Naskar, J.P. Garcia, M. Sommer, E. Kim, Y. Adam, P.G. Haydon, E.S. Boyden, A.E. Cohen, and C.G. Dulla. 2022. Neuronal activity drives pathway-specific depolarization of peripheral astrocyte processes. *Nat Neurosci*. 25:607–616.

38. Saminathan, A., J. Devany, A.T. Veetil, B. Suresh, K.S. Pillai, M. Schwake, and Y. Krishnan. 2021. A DNA-based voltmeter for organelles. *Nat. Nanotechnol.* 16:96–103.

39. Kralj, J.M., D.R. Hochbaum, A.D. Douglass, and A.E. Cohen. 2011. Electrical spiking in Escherichia coli probed with a fluorescent voltage indicating protein. *Science*. 333:345–348.

40. Benarroch, J.M., and M. Asally. 2020. The Microbiologist's Guide to Membrane Potential Dynamics. *Trends in Microbiology*. 28:304–314.

41. Goldman, D.E. 1943. POTENTIAL, IMPEDANCE, AND RECTIFICATION IN MEMBRANES. *Journal of General Physiology*. 27:37–60.

42. Chow, C.C., and J.A. White. 1996. Spontaneous action potentials due to channel fluctuations. *Biophysical Journal*. 71:3013–3021.

43. White, J.A., J.T. Rubinstein, and A.R. Kay. 2000. Channel noise in neurons. *Trends in Neurosciences*. 23:131–137.

44. Goldwyn, J.H., and E. Shea-Brown. 2011. The What and Where of Adding Channel Noise to the Hodgkin-Huxley Equations. *PLOS Computational Biology*. 7:e1002247.

45. Hübel, N., and M.A. Dahlem. 2014. Dynamics from Seconds to Hours in Hodgkin-Huxley Model with Time-Dependent Ion Concentrations and Buffer Reservoirs. *PLoS Computational Biology*. 10:e1003941.

46. Di Francesco, D., and D. Noble. 1997. A model of cardiac electrical activity incorporating ionic pumps and concentration changes. *Philosophical Transactions of the Royal Society of London. B, Biological Sciences*. 307:353–398.

47. Bezanilla, F. 1987. Single sodium channels from the squid giant axon. *Biophysical Journal*. 52:1087–1090.

48. Marty, A. 1981. Ca-dependent K channels with large unitary conductance in chromaffin cell membranes. *Nature*. 291:497–500.

49. Hales, T.G., J.I. Dunlop, T.Z. Deeb, J.E. Carland, S.P. Kelley, J.J. Lambert, and J.A. Peters. 2006. Common Determinants of Single Channel Conductance within the Large Cytoplasmic Loop of 5-Hydroxytryptamine Type 3 and α4β2 Nicotinic Acetylcholine Receptors*. *Journal of Biological Chemistry*. 281:8062–8071.

50. Mino, H., J.T. Rubinstein, and J.A. White. 2002. Comparison of Algorithms for the Simulation of Action Potentials with Stochastic Sodium Channels. *Annals of Biomedical Engineering*. 30:578–587.

51. White, J.A., R. Klink, A. Alonso, and A.R. Kay. 1998. Noise from voltage-gated ion channels may influence neuronal dynamics in the entorhinal cortex. *J. Neurophysiol.* 80:262–269.

52. Skaugen, E., and L. Walløe. 1979. Firing behaviour in a stochastic nerve membrane model based upon the Hodgkin—Huxley equations. *Acta Physiologica Scandinavica*. 107:343–363.

53. Schmid, G., I. Goychuk, and P. Hänggi. 2003. Channel noise and synchronization in excitable membranes. *Physica A: Statistical Mechanics and its Applications*. 325:165–175.

54. Barreto, E., and J.R. Cressman. 2011. Ion concentration dynamics as a mechanism for neuronal bursting. *J Biol Phys*. 37:361–373.

55. Hübel, N., E. Schöll, and M.A. Dahlem. 2014. Bistable Dynamics Underlying Excitability of Ion Homeostasis in Neuron Models. *PLOS Computational Biology*. 10:e1003551.

56. Ganley, I.G., K. Carroll, L. Bittova, and S. Pfeffer. 2004. Rab9 GTPase Regulates Late Endosome Size and Requires Effector Interaction for Its Stability. *Mol Biol Cell*. 15:5420–5430.

57. Koivusalo, M., B.E. Steinberg, D. Mason, and S. Grinstein. 2011. In situ Measurement of the Electrical Potential Across the Lysosomal Membrane Using FRET. *Traffic*. 12:972–982.

58. Scott, C.C., and J. Gruenberg. 2011. Ion flux and the function of endosomes and lysosomes: pH is just the start. *BioEssays*. 33:103–110.

59. Ishida, Y., S. Nayak, J.A. Mindell, and M. Grabe. 2013. A model of lysosomal pH regulation. *The Journal of General Physiology*. 141:705–720.

60. Grabe, M., H. Wang, and G. Oster. 2000. The Mechanochemistry of V-ATPase Proton Pumps. *Biophysical Journal*. 78:2798–2813.

61. Salzer, J.L. 1997. Clustering Sodium Channels at the Node of Ranvier: Close Encounters of the Axon–Glia Kind. *Neuron*. 18:843–846.

62. Somjen, G.G. 2001. Mechanisms of Spreading Depression and Hypoxic Spreading Depression-Like Depolarization. *Physiological Reviews*. 81:1065–1096.

63. Dreier, J.P. 2011. The role of spreading depression, spreading depolarization and spreading ischemia in neurological disease. *Nat Med*. 17:439–447.

64. Ciftci, D., G.H.M. Huysmans, X. Wang, C. He, D. Terry, Z. Zhou, G. Fitzgerald, S.C. Blanchard, and O. Boudker. 2020. Single-molecule transport kinetics of a glutamate transporter homolog shows static disorder. *Science Advances*. 6:eaaz1949.

65. Kosmidis, E., C.G. Shuttle, J. Preobraschenski, M. Ganzella, P.J. Johnson, S. Veshaguri, J. Holmkvist, M.P. Møller, O. Marantos, F. Marcoline, M. Grabe, J.L. Pedersen, R. Jahn, and D. Stamou. 2022. Regulation of the mammalian-brain V-ATPase through ultraslow mode-switching. *Nature*. 611:827–834.

66. Hodgkin, A.L., and A.F. Huxley. 1952. A quantitative description of membrane current and its application to conduction and excitation in nerve. *J Physiol*. 117:500–544.

67. Barreto, E., and J.R. Cressman. 2011. Ion concentration dynamics as a mechanism for neuronal bursting. *J Biol Phys*. 37:361–373.

68. Sherman, A., J. Rinzel, and J. Keizer. 1988. Emergence of organized bursting in clusters of pancreatic beta-cells by channel sharing. *Biophysical Journal*. 54:411–425.

69. Krishnan, G.P., and M. Bazhenov. 2011. Ionic dynamics mediate spontaneous termination of seizures and post-ictal depression state. *J Neurosci*. 31:8870–8882.

70. Chay, T.R., and J. Keizer. 1983. Minimal model for membrane oscillations in the pancreatic beta-cell. *Biophysical Journal*. 42:181–189.

71. Sherman, A., and J. Rinzel. 1991. Model for synchronization of pancreatic beta-cells by gap junction coupling. *Biophysical Journal*. 59:547–559.

72. Balbi, P., P. Massobrio, and J.H. Kotaleski. 2017. A single Markov-type kinetic model accounting for the macroscopic currents of all human voltage-gated sodium channel isoforms. *PLOS Computational Biology*. 13:e1005737.

73. Schmandt, N.T., and R.F. Galán. 2012. Stochastic-Shielding Approximation of Markov Chains and its Application to Efficiently Simulate Random Ion-Channel Gating. *Physical Review Letters*. 109.

74. Gillespie, D.T. 1977. Exact stochastic simulation of coupled chemical reactions. *J. Phys. Chem.* 81:2340–2361.

75. Grabe, M., and G. Oster. 2001. Regulation of Organelle Acidity. *The Journal of General Physiology*. 117:329–344.

76. Murk, J.L. a. N., B.M. Humbel, U. Ziese, J.M. Griffith, G. Posthuma, J.W. Slot, A.J. Koster, A.J. Verkleij, H.J. Geuze, and M.J. Kleijmeer. 2003. Endosomal compartmentalization in three dimensions: Implications for membrane fusion. *PNAS*. 100:13332–13337.

77. Farsi, Z., J. Preobraschenski, G. van den Bogaart, D. Riedel, R. Jahn, and A. Woehler. 2016. Single-vesicle imaging reveals different transport mechanisms between glutamatergic and GABAergic vesicles. *Science*. 351:981–984.

78. Daniels, R.W., C.A. Collins, K. Chen, M.V. Gelfand, D.E. Featherstone, and A. DiAntonio. 2006. A Single Vesicular Glutamate Transporter Is Sufficient to Fill a Synaptic Vesicle. *Neuron*. 49:11–16.

79. Mutch, S.A., P. Kensel-Hammes, J.C. Gadd, B.S. Fujimoto, R.W. Allen, P.G. Schiro, R.M. Lorenz, C.L. Kuyper, J.S. Kuo, S.M. Bajjalieh, and D.T. Chiu. 2011. Protein Quantification at the Single Vesicle Level Reveals That a Subset of Synaptic Vesicle Proteins Are Trafficked with High Precision. *J. Neurosci.* 31:1461–1470.

80. Upmanyu, N., J. Jin, H. von der Emde, M. Ganzella, L. Bösche, V.N. Malviya, E. Zhuleku, A.Z. Politi, M. Ninov, I. Silbern, M. Leutenegger, H. Urlaub, D. Riedel, J. Preobraschenski,

I. Milosevic, S.W. Hell, R. Jahn, and S. Sambandan. 2022. Colocalization of different neurotransmitter transporters on synaptic vesicles is sparse except for VGLUT1 and ZnT3. *Neuron*. 110:1483-1497.e7.